









CHARACTERIZATION OF JOVIAN HECTOMETRIC SOURCES WITH JUNO: STATISTICAL POSITION AND GENERATION BY SHELL-TYPE ELECTRONS

B. Collet^{1*} , L. Lamy^{2,1} , C. K. Louis³ , P. Zarka² ,
R. Prangé² , P. Louarn⁴ , A. Sulaiman⁵ , and W. S. Kurth⁶ 

*Corresponding author: brieuc.collet@lam.fr

Citation:

Collet et al., 2023, Characterization of Jovian hectometric sources with Juno: Statistical position and generation by shell-type electrons, *in Planetary, Solar and Heliospheric Radio Emissions IX*, edited by C. K. Louis, C. M. Jackman, G. Fischer, A. H. Sulaiman, P. Zucca, published by DIAS, TCD, pp. 211-225, doi: 10.25546/103095

Abstract

The Juno orbiter has been exploring the polar magnetosphere of Jupiter since mid-2016. Thanks to its unique polar trajectory, it has crossed regularly the northern and southern sources of auroral hectometric radiation, acquiring pioneer radio, magnetic and electron in situ measurements. By conducting a survey of the first 10 perijoves, we show evidence of a systematic spatial conjugacy between the crossed hectometric sources and the zone of diffuse aurora. In the framework of the electron Cyclotron Maser Instability (CMI), we used electron distribution functions measured by JADE-E to derive (i) the CMI expected growth rate, (ii) the associated electron energy and (iii) the emission frequency. We then compared these values to the wave properties measured by Waves. In addition to the two CMI sources of free energy already identified in the literature (loss cone and conics), we show that shell-type electrons of about 1 – 5 keV are driving emission below the electron cyclotron frequency (as at Earth and Saturn).

¹ Aix Marseille Univ., CNRS, CNES, LAM, Marseille, France

² LESIA, Observatoire de Paris, PSL, CNRS, SU/UPMC, UPD, 5 place Jules Janssen, 92195 Meudon, France

³ School of Cosmic Physics, DIAS Dunsink Observatory, Dublin Institute for Advanced Studies, Dublin, Ireland

⁴ IRAP, Université de Toulouse, CNRS, CNES, UPS, Toulouse, France

⁵ School of Physics and Astronomy, University of Minnesota, Minneapolis, MN 55455, USA

⁶ Department of Physics and Astronomy, University of Iowa, Iowa City, IA 52242, USA,

1 Introduction

Planetary auroral radio emissions are produced by wave amplification through the Cyclotron Maser Instability (CMI). This electron-wave resonance was theoretically proposed by Wu & Lee (1979) and Wu (1985) to account for the generation of the Auroral Kilometric Radiation (AKR). It was then validated in situ with space plasma measurements at Earth with Viking and FAST (Louarn, 1992), at Saturn with Cassini (Lamy et al., 2010; Mutel et al., 2010; Kurth et al., 2011) and, most recently, at Jupiter with Juno (Louarn et al., 2017, 2018; Louis et al., 2019). The CMI amplifies waves near the local cyclotron angular frequency $\omega_{ce} = 2\pi f_{ce}$ in low density ($\omega_{pe} \ll \omega_{ce}$) ($\omega_{pe}^2 = \frac{ne^2}{m\epsilon_0}$ is the plasma angular frequency), from out-of-equilibrium weakly relativistic electrons (typically a few keV). Indeed, the electron distribution function (EDF noted f_e) must display positive df_e/dv_{\perp} (where v_{\perp} stands for the electron velocity in the direction perpendicular to the local magnetic field vector). At Earth, loss cone EDF (Wu & Lee, 1979; Wu, 1985) were first thought to be the prominent CMI source of free energy before horseshoe (or shell, in 3D) EDF were shown to be a more efficient driver (Pritchett, 1984). At Jupiter, the magnetospheric dynamics is not governed by the same processes. The solar wind/magnetosphere interaction is marginal while the fast rotation and the Jupiter–satellite interactions play a major role. Loss cone and conic–driven CMI were shown to be efficient drivers of Hectometric auroral emissions (HOM) (Louarn et al., 2017, 2018). In parallel, Louis et al. (2019) identified 26 HOM source crossings by tracking radio emissions observed at frequencies between f_{ce} and $f_{ce} + 1\%$ over the first 15 perijoves. While the footprint of the HOM sources was statistically found to coincide with the expected locus of the UV auroral oval, their comparison with images of the UV aurorae simultaneously obtained by the Hubble Space Telescope (HST) at three occasions showed a non-exact correspondence, the radio sources being rather magnetically linked to the equatorial boundary of the main oval.

Mauk et al. (2020) and Sulaiman et al. (2022) identified 3 distinct zones. The Diffuse Aurora (Diff. A.), mapping to the Diffuse UV Aurora equatorward of the main oval, is characterized by small-scale field-aligned currents (FAC), Alfvén waves, and empty upward loss cone; Zone I (ZI), connected to the main auroral oval, is characterized by inverted-V, broadband acceleration, enhanced downward loss cone, and upward FAC. Finally, the poleward Zone II (ZII) displays an enhanced upward loss cone and bi-directional, although dominantly downward, FAC. In parallel, Allegrini et al. (2020) identified a recurrent peak of 3–30 keV electron flux consistent with the Diff. A. zone (Sulaiman et al., 2022).

In this study, we first survey the spatial location of the HOM sources over the first 10 Juno orbits and compare it to the position of Diff. A., ZI and ZII auroral regions (Section 3). We then investigate the generation of Jovian hectometric emissions below f_{ce} through a case study (Section 4).

2 Data set

Overall, we used measurements from the radio and plasma wave instrument Waves (Kurth et al., 2017), from the flux gate magnetometer MAG (Connerney et al., 2017) and from

the electron spectrometer JADE-E (McComas et al., 2017).

Waves measures electric fields over the radio frequency range using an electric dipole antenna with four receivers from 50 kHz to 41 MHz. Fast-Fourier Transforms (FFT) of the waveform signal were used to build high resolution time–frequency spectrograms (fft 4096 samples at 7 Msps). Waves measurements were also used to measure the electron density, and so f_{pe} , from the tracking of the cut-off of the O mode emission (Sulaiman et al., 2022). MAG magnetic measurements were used to derive the total magnetic field amplitude and so f_{ce} along the spacecraft trajectory.

JADE-E measures electrons between 0.1 and 95 keV. Its spatial coverage is ensured by 64 anodes oriented every 7.5° so that JADE-E observes 2/3 of the sky (due to a failed sensor) every second. However, as Juno is spinning with a 30 s rotation period, JADE-E samples all directions in this time interval. The temporal cadence of JADE-E measurements during the auroral passes was 1 s. During the first 10 perijoves, the spacecraft orientation was the most favorable for particle measurements, with the magnetic field vector being perpendicular to the Juno spin axis (Mauk et al., 2020; Allegrini et al., 2020; Sulaiman et al., 2022). This interval was therefore ideal to conduct a survey of JADE-E electrons. In strong magnetic fields, the electron measurements are significantly depleted for pitch angles near 90° (McComas et al., 2017). Hence, it is difficult to discuss the types of CMI unstable EDF whose main characteristics are at this pitch angle (trapped electrons). Moreover, when the electron flux physically varies at sub-second timescales, the measured signal significantly varies with a delay of 0.1 s between two consecutively sampled energy channels. Because of these limitations, the values of f_{pe} derived from JADE-E are generally a lower limit.

3 Statistical locus of the hectometric sources

Following the results of Louis et al. (2019), we compiled a list of hectometric sources (for which waveform measurements were available) identified by emissions below $f_{ce} + 1\%$. We then compared those to the position of the UV aurorae mapped by Juno/UVS and JRM09 magnetic field model (Connerney et al., 2018) with a current sheet model (Connerney et al., 1981), of the Diff. A./ZI/ZII and of the peak of 3-30 keV electron flux (Allegrini et al., 2020). As these articles focused on the first 10 perijoves, our study was restricted to this interval.

The results are summarized in Table 1. Overall, 17 out of 25 (68%) identified hectometric sources corresponded to intervals during which the < 30 keV electron flux dominates the total electron flux. For all the 9 perijoves studied by Mauk et al. (2020) (100%), we found hectometric sources in the Diff. A. and, in 2 cases (22%), also overlapped with ZI. No hectometric source was found to map to the ZII region.

This survey statistically confirms that hectometric sources lie along flux tubes mostly co-located with the equatorward boundary of the main oval and, more precisely, mostly with Diff. A. It also suggests the association of HOM sources with 3-30 keV electrons and that the highly energetic electrons are not efficiently producing CMI unstable EDF.

Table 1: Hectometric and decametric sources identified during the 10 first perijoves and associated auroral regions. The 2 first columns provide the perijove number and the date. The 3rd column is the detected emission frequency. Crosses in the 4th column indicate emissions falling below the local electron cyclotron frequency, (exact time interval given in an additional row). The 5th column specifies the component of the UV aurora connected to the source crossing. Column 6 specifies the presence of a peak flux for 3-30 keV electrons and their sense of propagation (upward \uparrow or downward \downarrow). Column 7 is a reminder of the classification proposed by Mauk et al. (2020). Blank cells represent cases with no identified acceleration zone or 3-30 keV e^- flux.

	Date (UTC)	f (MHz)	$f < f_{ce}$	UV aurora	<30 keV e^- flux	Acceleration zones
South						
PJ1	2016-08-27 13:29:00 to 13:31:00	5		Diff. A.	$\uparrow\downarrow$	Diff A.
	2016-08-27 13:30:25 to 13:30:45	5	X	Diff. A.	$\uparrow\downarrow$	Diff A.
PJ3	2016-12-11 17:36:29 to 17:37:22	6		Diff. A.	$\uparrow\downarrow$	
PJ4	2017-02-02 13:36:14 to 13:38:30	5		Diff. A.	$\uparrow\downarrow$	Diff A
	2017-02-02 13:36:31 to 13:37:30	5	X	Diff. A.	$\uparrow\downarrow$	Diff A
PJ5	2017-03-27 9:36:04 to 9:36:45	4		Diff. A.	\downarrow	
	2017-03-27 9:40:05 to 9:40:40	3.5		Diff. A.	$\uparrow\downarrow$	
PJ6	2017-05-19 6:50:00 to 6:54:30	3		Main Oval & Diff. A.	\downarrow	Diff A & ZI
	2017-05-19 6:51:45 to 6:52:30	3	X	Diff. A.	\downarrow	Diff A
PJ7	2017-07-11 2:30:10 to 2:34:00	5		Diff. A.	$\uparrow\downarrow$	
PJ8	2017-09-01 22:26:28 to 22:27:55	5		Diff. A.	\downarrow	Diff A & ZI
PJ9	2017-10-24 18:27:33 to 18:30:50	15		Diff. A.	No	
North						
PJ3	2016-12-11 16:24:01 to 16:26:17	5		Main Oval & Diff. A.	$\uparrow\downarrow$	
	2016-12-11 16:24:34 to 16:25:15	5	X	Main Oval & Diff. A.	No	
PJ4	2017-02-02 12:25:00 to 12:26:47	7		Diff. A.	No	
PJ5	2017-03-27 8:31:57 to 8:35:07	17-21		Diff. A.	No	
PJ6	2017-05-19 5:31:07 to 5:33:36	8		Main Oval & Diff. A.	\downarrow	
	2017-05-19 5:32:40 to 5:33:00	8	X	Diff. A.	No	
PJ7	2017-07-11 2:30:24 to 2:33:55	5.5		Diff. A.	$\uparrow\downarrow$	Diff A
PJ8	2017-09-01 21:16:12 to 21:18:30	6.5		Main Oval & polarward	\downarrow	
PJ9	2017-10-24 17:19:49 to 17:21:03	13		Main Oval & Diff. A.	\downarrow	
	2017-10-24 17:19:55 to 17:20:05		X	Main Oval & Diff. A.	\downarrow	
	2017-10-24 17:20:30 to 17:20:50		X	Main Oval & Diff. A.	No	
PJ10	2017-12-16 16:47:00 to 16:50:06	1.8		Main Oval & Diff. A.		Diff A
	2017-12-16 16:49:10 to 16:50:06		X	Main Oval & Diff. A.		Diff A

These results have been also presented by Al Saati et al. (2022) in the framework of a global analysis of the Jovian magnetosphere–ionosphere coupling.

4 Search for CMI unstable electron distributions and analysis of wave properties

4.1 Growth rate analysis

To resolve ambiguity in the search for crossed radiosources, we developed an approach tracking CMI-unstable EDF measured by JADE-E, as the criterion $f \leq f_{ce} + 1\%$ remains empirical. The electron measurements are first used to derive the CMI wave growth rate ω_i and the emission frequency f . The obtained wave properties are then compared to those observed by Waves.

The calculation of the wave growth rate derives from the CMI resonance condition dis-

played in Equation (1):

$$\omega = \frac{\omega_{ce}}{\Gamma} + k_{\parallel}v_{\parallel} \quad (1)$$

where ω is the wave angular frequency, $\Gamma^{-2} = 1 - \frac{v^2}{c^2}$ is the Lorentz factor, k is the wave number, v is the speed of resonant electrons, c is the speed of light and \parallel (rep. \perp) designates the direction parallel (resp. perpendicular) to the magnetic field direction.

Using the weakly-relativistic approximation $\Gamma^{-1} \approx 1 - \frac{1}{2}\frac{v^2}{c^2}$, the resonance condition transforms into the equation of a circle, the so-called resonance circle, with radius v_r and center $(v_0, 0)$ in the $(v_{\parallel}, v_{\perp})$ plane:

$$v_{\perp}^2 + (v_{\parallel} - v_0)^2 = v_r^2 \quad (2)$$

where $v_0 = \frac{k_{\parallel}c^2}{\omega_{ce}}$ and $v_r = c\left(\frac{k_{\parallel}^2c^2}{\omega_{ce}^2} - 2\left(\frac{\omega}{\omega_{ce}} - 1\right)\right)^{1/2} = \sqrt{v_0^2 - 2c^2\Delta\omega}$ with $\Delta\omega = \frac{\omega - \omega_{ce}}{\omega_{ce}}$. Waves are amplified whenever the wave growth rate computed along this resonance circle is positive.

The expression of the normalized growth rate $\gamma = \frac{\omega_i}{\omega_{ce}}$ is derived from the dispersion relation in X mode from Le Quéau et al. (1984), who assumed that the plasma is composed of one cold population at thermodynamic equilibrium and one non-thermal energetic (or hot) population. As a first approximation, we supposed that the density of hot electrons was the density of JADE-E electrons with an energy above 1 keV.

$$\gamma = \frac{\left(\frac{\pi}{2}\epsilon_h\right)^2}{1 + \left(\frac{\epsilon_c}{2\Delta\omega}\right)^2} c^2 \int_0^{\pi} d\theta v_r^2 \sin^2(\theta) \frac{\partial f_h}{\partial v_{\perp}}(v_0 + v_r \cos(\theta), v_r \sin(\theta)) \quad (3)$$

where $\epsilon_{\alpha} = \frac{\omega_{p\alpha}}{\omega_{ce}}$ where $\omega_{p\alpha}$ is the plasma frequency of the hot ($\alpha = h$) or cold ($\alpha = c$) electrons and f_h is the EDF of hot electrons. The demonstration of this formula is detailed in Appendix A. This expression is more general than those used by Louarn et al. (2017) and Mutel et al. (2010).

The growth rate is then calculated by integration of $\frac{\partial f_e}{\partial v_{\perp}}$ along the resonance circle.

To optimize the determination of $\frac{\partial f_h}{\partial v_{\perp}}$, we applied a bi-linear interpolation to the measured EDF smoothed over 8 adjacent pixels along both the velocity v and the pitch angle θ . In practice, for a given EDF, we calculated two sets of resonance circles. The first, aimed at testing shell-driven CMI, consists of 94 centered circles ($v_0 = 0$) with radius distributed logarithmically from 200 eV to 31 keV. The second, 3947 non-centered circles exploring the ranges $v_0 \in [0.2 \text{ keV}, 34 \text{ keV}]$ and $v_r \in \{[0.2v_0, 1.25v_0]\}$ with $v_r > 0.2 \text{ keV}$ and aimed at testing loss cone or any other positive $\frac{\partial f_e}{\partial v_{\perp}}$. The loss cone circles are identified by the criterion $|\theta_{chara} - \theta_{LC}| < 7.5^\circ$, with $\theta_{chara} = \text{Arctan}(v_r/v_0)$ the characteristic pitch angle and θ_{LC} the theoretic loss cone angle. The circles intercepting less than 20 JADE-E pixels or more than 13% pixels with negative values (due to incorrect background subtraction) were rejected. To avoid confusion with sub-second variations, we imposed to the centered resonance circles to yield positive growth rates for at least two contiguous radii. According to Hess et al. (2008), the wave properties are linked to the circle that leads to the maximal

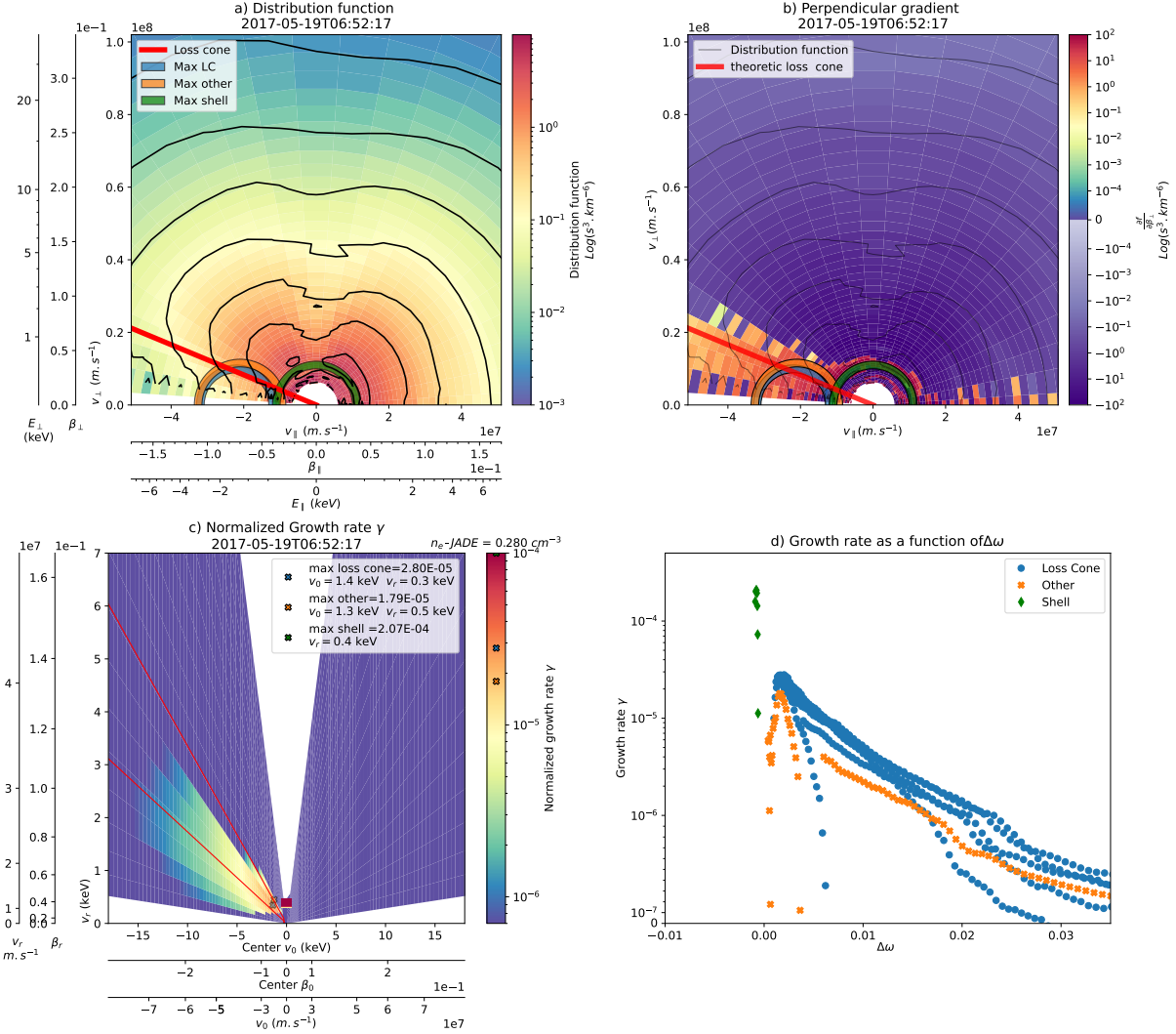


Figure 1: JADE-E data and growth rate at 6:52:17. a) JADE-E distribution function in $(v_{\parallel}, v_{\perp})$ phase space (converted in keV and in $\beta = \frac{v}{c}$ space) : black lines correspond to contours of a distribution function which is smoothed across 3 consecutive energy and pitch angles channels. The red line represents the theoretical loss cone computed from the JRM09 magnetic model. b) Computed $\frac{\partial f}{\partial v_{\perp}}$ in $(v_{\parallel}, v_{\perp})$ phase space. c) Computed growth rate (color scale) as a function of the center and radius of the corresponding resonance circle. The two red lines delimit the values where the circles are referred to as loss cone unstable resonance circles. d) Computed growth rate as a function of the difference from the local cyclotron frequency ($\Delta\omega = \frac{1}{2c^2}(v_0^2 - v_r^2)$). Green circles and diamonds represent shell unstable resonance circles, blue circles and dots represents loss cone unstable resonance circles and orange circles and stars represent other unstable resonance circles.

growth rate. We took into account the properties of the maximal growth rates of both sets to ensure comprehensive analysis.

Figure 1 illustrates the steps to derive γ on one sample of JADE-E measurement obtained on 2017-05-19 06:52:17 UT. Panel a) shows the JADE-E EDF in the phase space in color scale. The superimposed black lines plot isocontours of the smoothed EDF. Panel b) shows the computed perpendicular gradient of the EDF. On both panels, the red lines indicate the loss cone, while green, blue and orange circles are the most CMI unstable

ones (maximal growth rate) for each of the shell, loss cone and other types of circles, respectively. Panel c) plots the growth rate as a function of their radius and center of the resonance circles. Panel d) plots the growth rate as a function of $\Delta\omega$. The maximal growth rates of each type correspond to the circles plotted in panels a)-b). In this case, both a shell and loss cone resonance circle were CMI-unstable.

Through building a simple shell model, unaffected by the depletion effect, we evaluated that the growth rate computed from the observed (biased) EDF is underestimated by a factor 2.

4.2 Overview of the case of PJ6S

The sampling of PJ6S turned out to be an ideal case to investigate shell-type EDFs as source of free energy for CMI-driven hectometric emissions, as the Waves observations displayed emissions below f_{ce} which have not been investigated before. Moreover, the JADE-E spatial coverage was adequate (spacecraft orientation was most favorable to the particle instrument fields of view during the first perijoves).

Figure 2 presents an overview of radio and electron measurements on 19th May 2017. Panel a) shows a time frequency spectrogram of the flux density derived from Waves burst mode measurements. The black solid lines plot f_{ce} and $f_{ce} + 1\%$ while the vertical dashed lines mark the Diff. A./ZI/ZII regions (black) and the position of the main UV oval (blue). Radio emission is observed between f_{ce} and $f_{ce} + 1\%$ from 06:50:15 to 06:52:45 (black double arrow) (Diff. A and Zone I) and below f_{ce} from 6:51:45 to 6:52:30 (red double arrow). Panel b) displays f_{pe} as a function of time as derived from JADE-E (black) and Waves (blue) (Sulaiman et al., 2022) measurements, along with f_{ph} (red) the contribution for electrons above 1 keV. The latter dominates the plasma environment after 06:52. f_{pe} is much lower than f_{ce} throughout the interval with $f_{pe}/f_{ce} \sim 0.0015$ during the expected source crossing.

Figure 2 c) shows a JADE-E time–pitchangle spectrogram of the total electron flux between 1 and 10 keV. The black line indicates the loss cone. Figure 2 d)-e) present time–energy electron spectra from JADE-E for downward ($< 30^\circ$) (panel d) and upward ($> 150^\circ$) (panel e) electrons at all JADE-E energies (0.1 to 90 keV).

The electron density decreases with increasing latitude, whereas the density of hot electrons (in red) seems nearly constant until 6:53. This population of electrons is dominant from 6:52 to 6:53:30 where $\frac{n_{E>1\text{ keV}}}{n_{total}} > 0.6$. Moreover, the ratio $\frac{f_{pe}}{f_{ce}} \leq 5 \cdot 10^{-3} \ll 0.1$ fulfills the CMI condition.

An acceleration structure, differing from the inverted V signatures usually observed in terrestrial auroral regions, is visible between 06:52 and 06:53 (green double arrow). It consists of a depletion of electrons between 300 eV and 1 keV, best visible for the downward population (unaffected by the loss cone) while the density of electrons between 1 and 3 keV decreases at a lower rate.

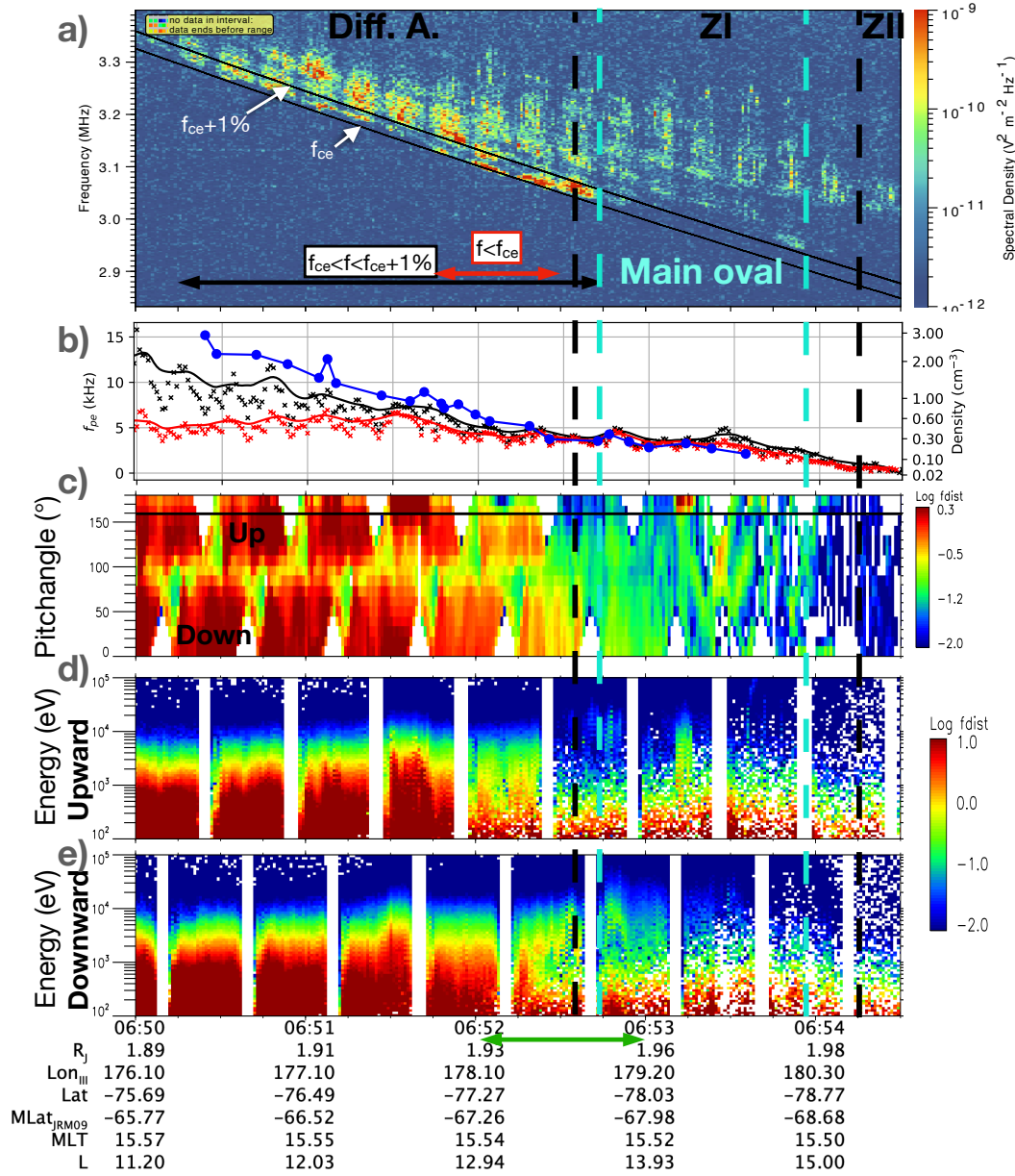


Figure 2: Juno radio and particle measurements obtained during PJ6S. (a) Time-frequency Waves spectrogram of Waves data (Burst mode, 4096 samples). The vertical black (blue) dashed lines delimit the auroral zones (the crossing of the main auroral UV oval, respectively). The two black solid lines plot f_{ce} and $f_{ce}+1\%$. (b) f_{pe} as a function of time, as derived from JADE-E (black) and from Waves (blue). The right-handed y axis displays the conversion in density units. The density of electrons ≥ 1 keV is displayed in red. The crosses plot individual JADE-E measurements, while the solid lines plot the 10s-average values of the upper envelope. (c) Time-pitch angle spectrogram of the electron flux sensed between 1 and 10 keV (d) Time-energy spectrogram of the downward electron flux ($< 30^\circ$) (e) Same as (d) for the upward electron flux ($> 150^\circ$).

4.3 Identification of CMI sources of free energy during PJ6S

We then applied our growth rate analysis to the same time interval (PJ6S, 06:50:00 to 06:54:30 UT) to compare the expected CMI wave properties to the measured ones.

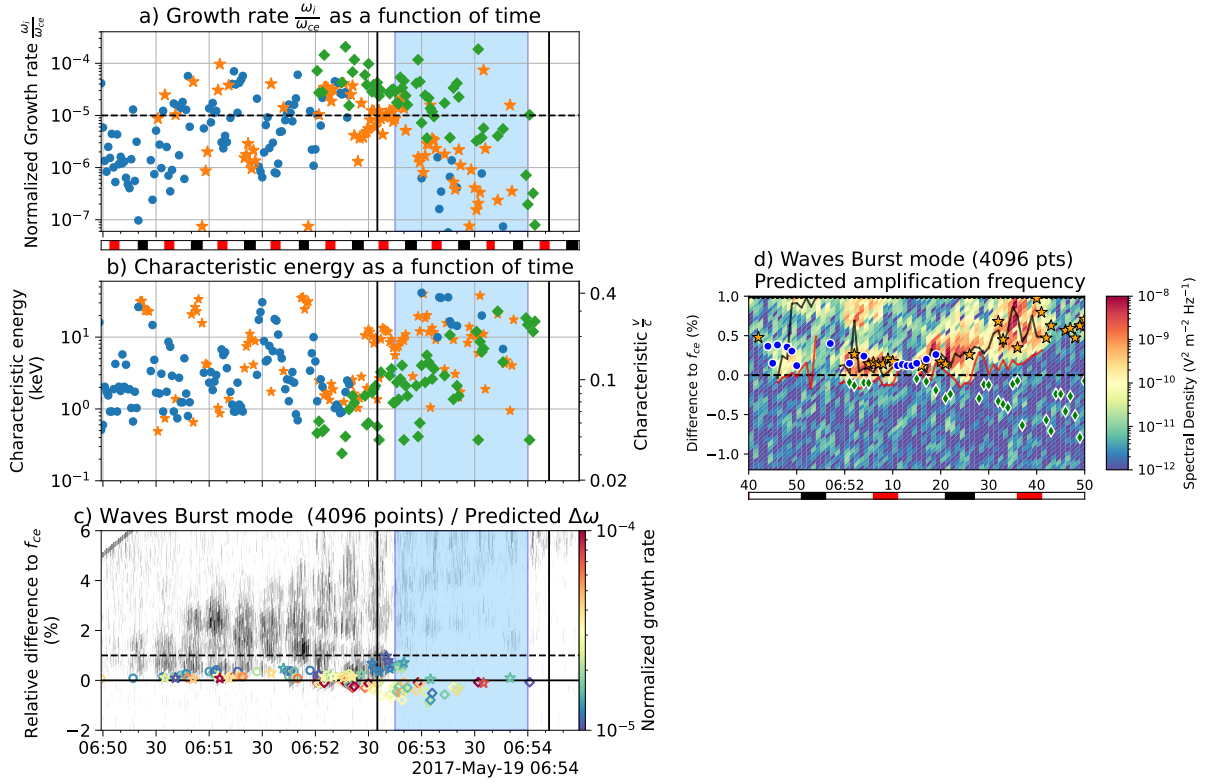


Figure 3: Growth rate analysis applied to the time interval of Figure 2. a) Maximum growth rate as a function of time. The blue dots represent the resonance circles nearly tangent to the loss cone, the green diamonds the shell-type circles (centered on 0) and the orange stars the other type of resonance circles. The blue zone indicates the crossing of the main UV auroral oval and the black lines mark the Diff. A/ZI/ZII frontiers. The colored axis below this panel indicates when JADE-E did not properly measure electrons in the upward direction (red, preventing the tracking of the loss cone) and in the downward direction (black). b) Characteristic energy derived from the resonance circles yielding the maximal growth rates as a function of time. c) Waves burst (4096 samples) dynamic spectrum. The superimposed colored symbols plot the emission frequency corresponding to the resonance circles yielding the maximal growth rates greater than 10^{-5} as a function of time. d) Zoom of panel c) during detection of emissions below f_{ce} . The black continuous line tracks the emission peak in the studied frequency range ($0.998 f_{ce}$ to $1.005 f_{ce}$) and the red line the low frequency cutoff (for emissions brighter than $10^{-11} V^2 m^{-2} Hz^{-1}$).

Figure 3 shows the maximal normalized growth rate γ as a function of time (panel a), its associated characteristic energy $E_{chara} = \frac{m_e}{2}(v_r^2 + v_0^2)$ (panel b) and predicted emission frequency superimposed. The plotted values are divided into three categories: the loss cone-type ones (blue dots), the shell-type ones (green diamonds), and the rest of circles inconsistent with the former two types (orange stars). Panel d displays a zoom of panel c over the interval 06:51:40 to 06:52:50 where emissions are detected below f_{ce} . For the sake of clarity, we plotted only the normalized growth rates above 10^{-5} (black dashed line in panel a)). There, the black solid line tracks the peak emission and the red solid line the hectometric low frequency cutoff.

Overall, JADE-E EDF yields positive CMI growth rates for all the categories of resonance circles all along the interval, with a peak of γ before the main oval crossing. The decrease of γ during ZI from 6:53:00 coincides with a significant decrease of the ratio of hot to cold electrons. Similarly, before 6:50:30, when there were no radio emissions below f_{ce} , the

growth rates are weak, whereas the density is high (though $\frac{\omega_{pe}}{\omega_{ce}} \ll 1$).

CMI-unstable loss cone EDFs are detected from 06:50:00 to 06:52:30, with γ_{LC} peaking near $4 \cdot 10^{-5}$ between 06:51:00 and 06:51:20 and between 06:52:00 and 06:52:20. This double peak corresponds to frequencies mapping to hectometric emissions observed slightly above f_{ce} (dots in panel c) and d)). The derived values of γ_{LC} correspond to CMI unstable electrons with $E_{chara} = 1 - 10$ keV.

CMI-unstable shell EDFs are detected over a smaller interval (06:52 to 06:54), which overlaps the acceleration structure described above. γ_{shell} peaks at 06:52:16 and at 06:52:46 (equatorward edge of ZI), reaching $\approx 1 \cdot 10^{-4}$ and $7 \cdot 10^{-5}$, respectively. The associated electron energies reach $E_{chara} \sim 0.5-2$ keV. Waves detected radio emissions below f_{ce} during the first peak, from 06:52:16 to 06:52:27. However, there are also high γ values for circles with $E_{chara} = 1-10$ keV electrons between 06:52:30 to 06:53:30, during which Waves did detect radio emissions but farther above f_{ce} .

Other CMI-unstable EDFs are detected at the same time as shell unstable EDF (6:52:00 and 6:52:25). These circles intercept upward electrons at larger pitch angles than the loss cone opening (orange circle Figure 1). This apparent enlargement of the loss cone characterized by the positive $\frac{\partial f_e}{\partial v_{\perp}}$ in the upward direction near the end of the shell section, can either be due to the loss cone that depletes the shell or to an incomplete adiabatic propagation of the shell or to conics. Moreover, these circles have characteristic energies similar to those of shell type EDFs (10 keV) but they correspond to wave amplification above ω_{ce} ($\Delta\omega \approx +0.5\%$). Other types of unstable EDFs, detected between 06:50 and 06:52 (when the loss cone was not sampled) and during the main auroral oval crossing, correspond to positive $\frac{\partial f_e}{\partial v_{\perp}}$ for downgoing electrons. These circles intercept high energy electrons (20-30 keV) and do not yield sufficiently high growth rates.

On panel d), a good correlation is again observed between the frequencies obtained from loss cone (blue dots) and other (orange stars) CMI-unstable EDF and the frequencies of observed peak emissions. Additionally, this closer analysis reveals emissions not detected by Waves due to its antenna orientation (between 6:52:10 and 6:52:15) due to the spin of Juno. The shell circle radii are consistent with the observed frequencies. Beyond 6:52:30, we observe shell but no emissions, as discussed earlier. Overall, the results from panels c) and d) support a strong correlation between CMI predictions and detected radio emissions.

4.4 Discussion

Three CMI-unstable electron populations coexisted during PJ6S, yielding emission simultaneously radiated at slightly different frequencies. We first confirmed loss cone-type EDF as the prominent source of free energy. We did not observe the conics identified by Louarn et al. (2018) over the same perijove, who used a biased older version of the JADE-E calibration pipeline. The newly identified shell-type EDF is scarcely observed suggesting that electron beams form a secondary CMI source of free energy at Jupiter. In the Diff. A., resonance circles corresponding to very low energy electron beams (0.5-2 keV) coincided with lower frequency cutoffs for HOM emissions below f_{ce} (down to 0.5%). During

the main auroral oval crossing, shell-type circles corresponding to higher energy electron beams (1-10 keV, more usually observed at Earth/Saturn) were inferred from JADE-E and led to high growth rates. However, Waves did not detect any radio counterpart at the expected frequencies (down to -1%), possibly because the wave flux density was too low. We hypothesize that the latter population correspond to smaller-size sources at specific frequencies leading to too short interaction time with the waves. We note that, in this interval, the EDF presents a saw tooth profile (not shown here) suggesting small-scale variations below JADE-E 1 s time resolution supporting this hypothesis.

The coexistence of different CMI sources of free energy has another important implication. Since multiple portions of the EDF can be unstable simultaneously, the electron–wave energy conversion efficiency is likely larger than the typical 1% reference value derived at Earth/Saturn. The quantitative determination of the final wave flux density and the associated energy conversion efficiency are beyond the scope of this paper.

Our work also suggests that radio emissions are strongly linked with the physical processes at stake in Diff. A. This is the zone where Alfvénic fluctuations are most strongly observed compared to ZI and ZII (Sulaiman et al., 2022) and since shell-type EDFs can be generated by Alfvén waves (Hess et al., 2007), we expect that observed shell distributions are generated by these waves.

In this work, we used a more general expression of the CMI growth rate than Mutel et al. (2010) and Louarn et al. (2017). The two previous expressions can be retrieved from ours by assuming that ϵ_c is smaller or larger than $\Delta\omega$. For the studied interval, ϵ_c is generally below $\Delta\omega$ except for circles below 3 keV where $\epsilon_c > 0.2\Delta\omega$, meaning that the Mutel et al. formula is more suitable. Indeed, applying Louarn et al.’s formula on our assumptions yields γ values 10 times higher and tends to select high energy electrons. This formula was derived from Le Quéau et al. (1984)’s dispersion relation but one might achieve an even more precise growth rate formula by recalculating the conductivity tensor as Wu (1985) did but for conditions at Jupiter, where hot electrons are dominant.

5 Conclusions and perspectives

In this study, we showed that the Jovian HOM sources are statistically colocated with the diffuse UV aurorae equatorward of the main oval and mostly in the Diff. A. zone from Mauk et al. (2020) (100%) and in the < 30 keV peak of electron flux from Allegrini et al. (2020) (68%). This supports the prominent role of Alfvén waves and small scale currents under 30 keV in generating CMI-unstable EDFs at Jupiter.

Through a CMI growth rate analysis based on EDF measurements, we then provide the first evidence of shell-driven (0.5 to 2 keV, $\Delta f \gtrsim -0.5\%$) HOM emission below f_{ce} at Jupiter, which coexists with emissions above f_{ce} driven by loss cone type (1-10 keV, $\Delta f < +0.5\%$) and other types of EDF (0.5-2 eV, $\Delta f < +0.5\%$ and $\gtrsim 10$ keV, $\Delta f + 0.5 - 1\%$).

These results now deserve to be checked statistically to assess the properties of the radio sources and the CMI generation mechanisms over a broader range of local times. It will

also be interesting to evaluate the role of the recurring Alfvénic fluctuations in Diff. A. Such work is beyond the scope of this paper.

Acknowledgments

The authors acknowledge support from CNES and from CNRS/INSU programs of Planology (PNP) and Heliophysics (PNST) and thanks E. Penou for the help with the particle analysis through the CLWeb software. The research at the University of Iowa is supported by NASA through Contract 699041X with the Southwest Research Institute. WSK acknowledges the use of the Space Physics Data Repository at the University of Iowa supported by the Roy J. Carver Charitable Trust. C. K. Louis' work at the Dublin Institute for Advanced Studies was funded by the Science Foundation Ireland Grant 18/FRL/6199. We used calibrated JADE-E data from CLweb software (IRAP), this data and other Juno data used in this work are publicly available from NASA's Planetary Data System.

A Derivation of the growth rate

To obtain a relation of dispersion for the CMI, Le Quéau et al. (1984) made key assumptions: $\frac{\omega_{pe}}{\omega_{ce}} \ll 1$, the plasma is composed of two electron populations, one cold population at thermodynamic equilibrium and one non thermal energetic (or hot) population. This hot population is considered weakly relativistic, such as $\Gamma^{-1} = \sqrt{1 - \frac{v^2}{c^2}} \approx 1 - \frac{v^2}{2c^2}$ and $\Gamma \frac{k_{\perp} v_{\perp}}{\omega_{ce}} \ll 1$. The amplified wave is emitted in RX mode close to the cyclotron frequency $\omega \approx \omega_{ce}$, in a quasi perpendicular direction $k_{\parallel} \ll k$. From the relativistic form of the dispersion matrix, we can derive the following dispersion relation

$$D = 1 - \frac{k^2 c^2}{\omega^2} + \left(1 - \frac{k_{\perp}^2 c^2}{2\omega^2}\right) (J_h + J_c) = 0 \quad (\text{A1})$$

$$J_c = -\frac{\omega_{pc}^2}{(\omega - \omega_{ce})\omega} \quad ; \quad J_h = \frac{\pi\omega_{ph}^2}{\omega^2} \int_{-\infty}^{\infty} dv_{\parallel} \int_0^{\infty} dv_{\perp} v_{\perp}^2 \omega \frac{\partial f_h}{\partial v_{\perp}} \left(\omega - k_{\parallel} v_{\parallel} - \omega_{ce} \left(1 - \frac{v^2}{2c^2}\right) \right)^{-1}$$

Where f_h is the normalized distribution function of the hot electrons in the phase space such as $\int dv^3 f_h = 1$, $\omega_{p\alpha}$, J_{α} for $\alpha \in \{c, h\}$ represent the plasma frequency and the current contribution of cold ($\alpha = c$) and hot ($\alpha = h$) electrons. The expression within parenthesis is the resonance equation mentioned above.

Using Plemelj formula $\int_{-\infty}^{+\infty} \frac{f(x)}{x-x_0} dx = P.V \int_{-\infty}^{+\infty} dx f(x) + i\pi \int_{-\infty}^{+\infty} dx f(x) \delta(x-x_0)$, with $P.V.$ the Cauchy principal value, Le Quéau et al. obtained $Im(J_h)$:

$$\begin{aligned}
Im(D) &= -\frac{\pi^2 \omega_{ph}^2}{2\omega^2} \int_{-\infty}^{\infty} dv_{\parallel} \int_0^{\infty} dv_{\perp} v_{\perp}^2 \omega \frac{\partial f_h}{\partial v_{\perp}} \delta \left(\omega - k_{\parallel} v_{\parallel} - \omega_{ce} \left(1 - \frac{v^2}{2c^2} \right) \right) \quad (A2) \\
&= -\frac{\pi^2 \omega_{ph}^2}{\omega_{ce}^2} c^2 \int_0^{\pi} d\theta v_r^2 \sin^2(\theta) \frac{\partial f_h}{\partial v_{\perp}} (v_0 + v \cos(\theta), v \sin(\theta)) \delta(v^2 - v_r^2) \\
&= -\frac{\pi^2 \omega_{ph}^2}{2\omega_{ce}^2} c^2 \int_0^{\pi} d\theta v_r^2 \sin^2(\theta) \frac{\partial f_h}{\partial v_{\perp}}
\end{aligned}$$

They also neglected $Re(J_h)$ in front of J_c in the expression of $Re(D)$ (which could be further debated since at Jupiter, hot electrons dominate). Supposing $\frac{kc}{\omega} \approx \frac{k_{\perp}c}{\omega} \approx 1$, we obtain the following :

$$\begin{aligned}
\frac{\partial}{\partial \omega} Re(D) &= \frac{\partial}{\partial \omega} \left(1 - \frac{k^2 c^2}{\omega^2} + J_c \left(1 - \frac{k_{\perp}^2 c^2}{2\omega^2} \right) \right) \quad (A3) \\
&= \frac{2k^2 c^2}{\omega^3} - \frac{k_{\perp}^2 c^2 \omega_{pc}^2}{\omega^2 \omega_{ce} \Delta \omega} + \frac{\omega_{pc}^2 \frac{\omega_{ce}}{\omega} \Delta \omega + 1}{\omega^2 \omega \Delta \omega^2} \left(1 - \frac{k_{\perp}^2 c^2}{2\omega^2} \right) \\
&= \frac{2}{\omega_{ce}} + \frac{\omega_{pc}^2}{\omega_{ce}^2} \frac{1}{2\omega_{ce} \Delta \omega^2} = \frac{2}{\omega_{ce}} \left(1 + \left(\frac{\epsilon_c}{2\Delta \omega} \right)^2 \right)
\end{aligned}$$

This expression was obtained by setting $\omega \approx \omega_{ce}$, $\Delta \omega \ll 1$ and $\epsilon_c = \frac{\omega_{pc}}{\omega_{ce}}$. Using $\omega_i = -Im(D) \left(\frac{\partial Re(D)}{\partial \omega} \right)^{-1}$, we obtain the following growth rate expression:

$$\gamma = \frac{\omega_i}{\omega_{ce}} = \frac{\left(\frac{\pi \epsilon_h}{2} \right)^2}{1 + \left(\frac{\epsilon_c}{2\Delta \omega} \right)^2} c^2 \int_0^{\pi} d\theta v_r^2 \sin^2(\theta) \frac{\partial f_h}{\partial v_{\perp}} (v_0 + v_r \cos(\theta), v_r \sin(\theta)) \quad (A4)$$

For $\Delta \omega \ll \frac{\epsilon_c}{2}$, we retrieve Louarn et al.'s expression : $\gamma \approx \frac{\pi^2 n_h}{n_c} \Delta \omega^2 c^2 \int_0^{\pi} d\theta v_r^2 \sin^2(\theta) \frac{\partial f_h}{\partial v_{\perp}}$, and for $\Delta \omega \gg \frac{\epsilon_c}{2}$, we retrieve Mutel et al.'s expression $\gamma \approx \left(\frac{\pi \omega_{ph}}{2\omega_{ce}} \right)^2 c^2 \int_0^{\pi} d\theta v_r^2 \sin^2(\theta) \frac{\partial f_h}{\partial v_{\perp}}$

It is important to notice there that f_h is normalized such that $\int dv^3 f_h = 1$ ($s^3 m^{-3}$) whereas the plotted EDF in Figure 1 are normalized such that $\int dv^3 f_h = n$ ($s^3 km^{-6}$) and the plotted gradient $\frac{\partial f}{\partial \beta_{\perp}}$ has the same unit as f since $\beta_{\perp} = \frac{v_{\perp}}{c}$.

References

- Al Saati S., et al., 2022, Magnetosphere–ionosphere–thermosphere coupling study at Jupiter based on Juno's first 30 orbits and modeling tools, *Journal of Geophysical Research: Space Physics*, 127, e2022JA030586
- Allegrini F., et al., 2020, Energy flux and characteristic energy of electrons over jupiter's main auroral emission, *Journal of Geophysical Research: Space Physics*, 125, e2019JA027693

- Connerney J. E. P., Acuna M. H., Ness N. F., 1981, Modeling the Jovian current sheet and inner magnetosphere, *Journal of Geophysical Research: Space Physics*, *86*, 8370
- Connerney J. E. P., et al., 2017, The Juno Magnetic Field Investigation, *Space Science Reviews*, *213*, 39
- Connerney J. E. P., et al., 2018, A new model of Jupiter's magnetic field from Juno's first nine orbits, *Geophysical Research Letters*, *45*, 2590
- Hess S., Mottez F., Zarka P., 2007, Jovian S burst generation by Alfvén waves, *Journal of Geophysical Research: Space Physics*, *112*, A11212
- Hess S., Cecconi B., Zarka P., 2008, Modeling of Io–Jupiter decameter arcs, emission beaming and energy source, *Geophysical Research Letters*, *35*, L13107
- Kurth W. S., et al., 2011, A Close Encounter with a Saturn Kilometric Radiation Source Region, in *Planetary Radio Emissions VII*, eds Rucker H. O., Kurth W. S., Louarn P., and Fischer G., pp 75–85
- Kurth W. S., et al., 2017, The Juno Waves Investigation, *Space Science Reviews*, *213*, 347
- Lamy L., et al., 2010, Properties of Saturn kilometric radiation measured within its source region, *Geophysical Research Letters*, *37*, L12104
- Le Quéau D., Pellat R., Roux A., 1984, Direct generation of the Auroral Kilometric Radiation by the maser synchrotron instability: Physical mechanism and parametric study, *Journal of Geophysical Research: Space Physics*, *89*, 2831
- Louarn P., 1992, Auroral planetary radio emissions, theoretical aspects, *Advances in Space Research*, *12*, 121
- Louarn P., et al., 2017, Generation of the Jovian hectometric radiation: First lessons from Juno, *Geophysical Research Letters*, *44*, 4439
- Louarn P., et al., 2018, Observation of electron conics by Juno: Implications for radio generation and acceleration processes, *Geophysical Research Letters*, *45*, 9408
- Louis C., Prangé R., Lamy L., Zarka P., Imai M., Kurth W., Connerney J., 2019, Jovian Auroral Radio Sources Detected In Situ by Juno/Waves: Comparisons With Model Auroral Ovals and Simultaneous HST FUV Images, *Geophysical Research Letters*, *46*, 11606
- Mauk B. H., et al., 2020, Energetic particles and acceleration regions over jupiter's polar cap and main aurora: A broad overview, *Journal of Geophysical Research: Space Physics*, *125*, e2019JA027699
- McComas D. J., et al., 2017, The Jovian Auroral Distributions Experiment (JADE) on the Juno mission to Jupiter, *Space Science Reviews*, *213*, 547

Mutel R. L., et al., 2010, CMI growth rates for Saturnian kilometric radiation, *Geophysical Research Letters*, 37, L19105

Pritchett P. L., 1984, Relativistic dispersion and the generation of auroral kilometric radiation, *Geophysical Research Letters*, 11, 143

Sulaiman A. H., et al., 2022, Jupiter's low-altitude auroral zones: Fields, particles, plasma waves, and density depletions, *Journal of Geophysical Research: Space Physics*, 127, e2022JA030334

Wu C. S., 1985, Kinetic cyclotron and synchrotron maser instabilities: Radio emission processes by direct amplification of radiation, *Space Science Reviews*, 41, 215

Wu C. S., Lee L. C., 1979, A theory of the terrestrial kilometric radiation, *Astrophysical Journal*, 230, 621